NJC

ROYAL SOCIETY OF CHEMISTRY

PAPER

View Article Online
View Journal | View Issue

Check for updates

Cite this: *New J. Chem.*, 2021, 45, 6760

Chromene–triazole-pyrimidine based chemosensor therapeutics for the *in vivo* and *in vitro* detection of Fe^{3+} ions†

Aranhikkal Shamsiya and Damodaran Bahulayan *

Received 24th November 2020,
Accepted 13th March 2021

DOI: 10.1039/d0nj05697a

rsc.li/njc

The development of a series of chromene–pyrimidine triad molecules for the selective detection of Fe^{3+} is described. The new chemosensors were synthesized through the sequential use of multicomponent reactions (MCRs) and click chemistry marking its ease and cost effectiveness. The sensor molecules showed turn-off fluorescence towards Fe^{3+} with an extremely low limit of detection (LOI) and a strong affinity to cancer causing CDK2 proteins with binding energy closer to −9.8 kcal mol^{-1} as indicated by the molecular docking studies. The free hydrophilic handles present on the sensors are advantageous for binding with cellular Fe^{3+} demonstrating the potential of these molecules as therapeutics for iron overloading diseases. The therapeutic potential is further illustrated *via* cytotoxicity studies against the human cervical cancer cell line HeLa, which showed a very low IC50 value of 15 μg mL^{-1}.

Published on 15 March 2021. Downloaded by University of New Mexico on 5/16/2021 5:31:46 PM.

Introduction

Iron is one of the important elements that regulate many metabolic processes in the human body.[1] Iron can act as both electron donor and acceptor by changing the oxidation states from Fe(II)–Fe^{2+}, Fe(III)–Fe^{3+}, and Fe(IV)–Fe^{4+}. Such electron transfer properties enable it to be a catalyst for many biochemical reactions. Among the various oxidation states of iron, Fe^{3+} plays a vital role in cellular events such as DNA replication, oxygen transport,[2,3] *etc.* However, deficiency or excess of iron in the human metabolism may cause either iron-deficiency anemia or iron-loading anemia leading to various forms of cancers, heart ailments, diabetes, liver disease, osteoarthritis, osteoporosis,[4–6] neurodegenerative disorders, Alzheimer's disease[7] and Parkinson's disease.[8,9] Consequently, metabolic iron has become an important target in drug discovery for a broad spectrum of chronic diseases. A variety of small molecules based fluorescent probes have been developed in the recent past as Fe^{3+} sensors based on either fluorescence turn on or quenching mechanisms.[10] These probes were featured with a hydrophilic iron binding handle, receptor binding pocket, and a fluorophore for signaling. Common fluorophores include coumarin, anthracene, naphthalene, fluorescein, pyrene, rhodamine, *etc.* and the receptor binding pocket can be a polypeptide, polyamine, or calixarene type supermolecules. The binding handle, receptor binding unit, and fluorophores were assembled *via* multistep synthesis. Although the majority of the iron sensors developed so far show promising applications, there is still a need for the development of more biocompatible Fe^{3+} sensors/therapeutic agents for the complexation induced (i) therapy for diseases like iron-loading anemia, (ii) drinking water purification, *etc.*

We have recently developed novel fluorescent probes based on coumarin[11] and pyrimidine[12] for the selective and sensitive detection of Fe^{3+} and azide ions respectively. In continuation of our research to develop more biocompatible fluorescent probes, here we report the design and synthesis of an array of new Fe^{3+} sensors and their cytotoxicity against the human cervical cancer cell line (HeLa). The new sensor/probes were assembled through the integration of the biological base pyrimidine with a naturally occurring chromene moiety using efficient and economic synthetic protocols like multicomponent reactions[13,14] and click chemistry.[15,16]

Experimental section

General procedure for the Cu(I) catalyzed (3+2) azide–alkyne 1,3-dipolar cycloaddition reactions for the synthesis of chromene-pyrimidinone triazole CP1

An equimolar mixture of azide P1 (1 mmol) and the alkyne (C1, 1 mmol) was mixed with 0.2 equiv. of $CuSO_4$ and 0.4 equiv. of sodium ascorbate in a mixed solvent system containing tert-butanol, water, and DMSO (4 : 2 : 1) at room temperature. After 12 h, the reaction mixture was diluted with cold water to afford the substituted triazoles in the solid form. The solid obtained was washed with water to obtain **CP1** in the pure form.

Department of Chemistry, University of Calicut, Malappuram 673635, Kerala, India. E-mail: bahulayan@yahoo.com, cue2994@uoc.ac.in

† Electronic supplementary information (ESI) available: Experimental details and compound characterization. See DOI: 10.1039/d0nj05697a

 This journal is © The Royal Society of Chemistry and the Centre National de la Recherche Scientifique 2021

Published on 15 March 2021. Downloaded by University of New Mexico on 5/16/2021 5:31:46 PM.

Brown solid. Mp 145–147 °C, yield 85%; ^{1}H NMR (500 MHz, DMSO): δH (ppm): 8.57 (s, 2H), 7.85–7.22 (m, 14H), 7.58 (s, 1H), 6.21 (s, 2H), 5.96 (s, 1H), 5.52 (s,1H), 5.23–5.11 (d,1H), 5.02 (s, 2H), 4.30 (s, 2H), 4.15–4.09 (q, 2H), 1.35–1.31 (t, 3H); ^{13}C NMR (DMSO-(d6), 500 MHz): 35.80, 39.50, 39.67, 39.83, 40.00, 40.17, 40.26, 40.33, 40.42, 40.50, 40.59, 55.79, 71.25, 79.45, 80.32, 81.00, 104.50, 114.73, 115.79, 116.21, 116.42, 123.78, 124.43, 128.15, 131.83, 132.15, 133.64, 152.76, 158.16, 165.13, 171.23; FT-IR (KBr) (ν_{max}, cm^{-1}: 3383, 2928, 2227, 1697, 1552, 1504, 1512, 1487, 1457, 1369, 1307, 1227, 1175, 1097, 1030, 756); HRMS *m*/*z* calcd for $C_{37}H_{31}N_7O_6$ $[M]^+$: 669.23358, found: $[M]^+$: 669.23352.

Results and discussion

Design strategy

Our probe design strategy consists of mainly three synthetic stages: (i) synthesis of the chromene with an alkyne functionality (ESI,† Scheme S1), (ii) synthesis of the pyrimidines with an azide functionality (ESI,† Scheme S2) and (iii) the final assembly of the probe molecules by connecting the chromenes with the pyrimidines through a spacer triazole *via* the alkyne-azide (2+3) click cycloaddition (Scheme 1). Scheme S1 (ESI†) presents a base catalyzed three component reaction between naphthalene, an alkyne functionalized aldehyde, and malononitrile at 80 °C which afforded the chromene alkynes in a quantitative yield. The azide functionalized pyrimidines were synthesized *via* the classical Biginelli multicomponent reaction of benzaldehydes with urea and an active methylene compound and the subsequent chlorine substitution with an azide functionality as shown in Scheme S2 (ESI†). Both steps involved in Scheme S2 (ESI†) have proceeded nicely with the formation of the chloro and azido pyrimidines in excellent yield and purity. The chromene and pyrimidine fragments were then assembled through copper catalyzed azide–alkyne (3+2) cycloaddition (CuAAC), as shown in Scheme 1 to obtain the probes **CP1–CP6** as listed in Scheme 2.

Solution state fluorescence

The photophysical properties of these new probes were evaluated by measuring the absorption, emission, and fluorescence quantum yields in the solution state, and the values are summarized in Table 1.

All 6 compounds showed fluorescence in the blue region with a large Stokes shift and high quantum yield. The emission properties of the molecules were related to the presence of electron transfer from the HOMO to the LUMO of the molecules. The HOMO of the molecule is located in the coumarin core and it acts as an electron donor (D) whereas the LUMO of the molecule is located in the dihydropyrimidinone moiety and it acts as electron acceptor (A). Hence there is an electron donor–acceptor interaction possible in the molecule due to intramolecular charge transfer (ICT). The electron is excited to the LUMO and subsequently relaxes to the ground state causing blue emission from the molecule. The normalized absorption and emission spectra of **CP1–CP6** are present in Fig. 1.

Solid-state fluorescence

The fluorescence of these molecules showed a redshift in the solid (aggregated) state. A variety of variables are believed to contribute to the generation of aggregation induced emission (AIE) and aggregation induced enhanced emission (AIEE). These variables include the restriction of charge transfer (CT), intramolecular rotation (RIR), intermolecular interaction, *etc.*[17,18] The restriction of the intramolecular motion of the compound in the aggregated state could be the reason for the aggregation-induced emission enhancement (AIEE) for weakly fluorescent molecules.[19–28] The solid-state absorption and emission of the molecules are **CP1–CP6** depicted in Fig. 2.

Sensor properties

Since **CP1–CP6** have similar photophysical properties with comparable Stokes shifts and quantum yields, the variation in the fluorescence intensity of these probes in the presence of various analytes (Fe^{3+}, Cu^{2+}, Cd^{2+}, Hg^{2+}, Ca^{2+}, Mg^{2+}, Mn^{2+}, Zn^{2+}, Co^{2+}, Pb^{2+}, Na^+, Ni^{2+}) were evaluated using **CP1** as the model compound.

Among the various metal ions tested, the addition of Fe^{3+} to the **CP1** in DMSO showed significant variations in the absorbance and fluorescence intensity, unlike other analytes and a significant fluorescence turn-off behavior as shown in Fig. 3 and 4. The fluorescence titration was carried out by adding an aqueous solution of Fe^{3+} ions (0.01 mM) into **CP1** (1.0×10^{-4} M) in DMSO. The fluorescence intensity of **CP1** showed a gradual decrease upon increasing the concentration of Fe^{3+} from 0 to 0.5 equivalents. From the Stern–Volmer emission spectral profile (concentration *versus* fluorescence intensity) given in the inset of Fig. 4b, the limit of detection (LOD) of the chemosensor **CP1** for Fe^{3+} was determined to be 0. 14 μM. The association constant (K_a) was also obtained from the fluorescence titration. The low value obtained for the LOD reveals that the new probe **CP1** can be used for the

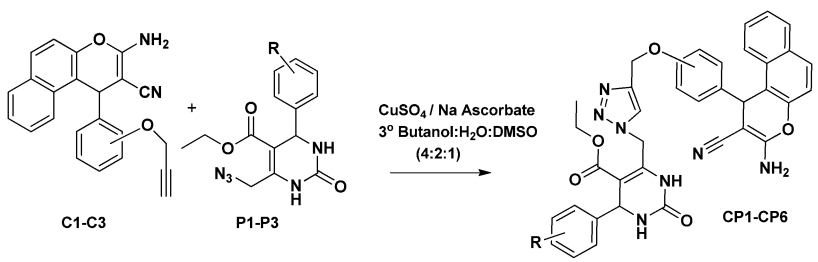

Scheme 1 Cu(I) catalyzed (2+3) alkyne-azide cycloaddition (click chemistry) assisted synthesis of chromene–pyrimidinone triads.

Published on 15 March 2021. Downloaded by University of New Mexico on 5/16/2021 5:31:46 PM.

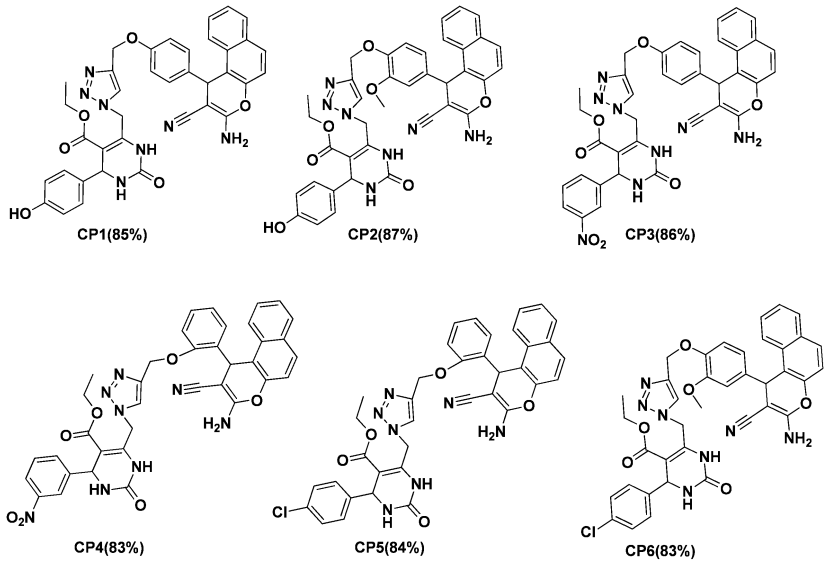

Scheme 2 List of chromene–triazole-pyrimidine chemosensors prepared.

Table 1 Absorption maxima (nm), emission maxima (nm), and the quantum yield of **CP1–CP6**

Entry	Abs_{max}	$Emis_{max}$	Stokes shift	Quantum yield
CP1	371	472	101	0.316
CP2	370	463	93	0.440
CP3	352	459	107	0.235
CP4	369	465	96	0.370
CP5	370	471	101	0.327
CP6	360	459	99	0.315

in vitro/*in vivo* detection of micromolar level iron present in various entities.

To determine the stoichiometric ratio between **CP1** and Fe^{3+}, the method of continuous variation (Job's plot) was adopted. The total concentration of the receptor **CP1** and ions Fe^{3+} were kept constant (1.0×10^{-4} M) with continuous variation of the mole fraction of **CP1** ([receptor]/[receptor] + [ion]). Fig. 5a shows the Job's plots of **CP1** with Fe^{3+}. When the mole fraction of CP1 was 0.5, the receptors **CP1**–Fe^{3+} complex concentration attained a maximum. This indicated the formation of a 1.1 complex of **CP1** with Fe^{3+}. This 1 : 1 interaction was also confirmed from the Benesi–Hildebrand (B–H) plot.[29,30] B–H plot is a statistical method used for the determination of the equilibrium constant *K* and stoichiometry of non-bonding interactions in the complexes. The Benesi–Hildebrand (B–H) plot, in this case, was obtained as a linear plot validating the assumption of 1 : 1 stoichiometry. The data obtained from multiple spectrofluorometric titrations were used for the B–H calculations and the equilibrium constant was obtained as a $5.36 \pm 0.09 \times 10^6$ unit (Fig. 5b). The higher value obtained for the equilibrium constant reveals the strong binding of **CP1** with Fe^{3+} to form a stable complex.

Mechanism of the turn off fluorescence

To derive a possible mechanism of fluorescence quenching, we have carried out the Density Functional Theory (DFT) calculations using the Gaussian 09[31] programme. For this, the **CP1** was optimized with DFT/B3LYP-6-31+G(d,p) while the **CP1**–Fe complex was analyzed by DFT/B3LYP-LANL2DZ.[32]

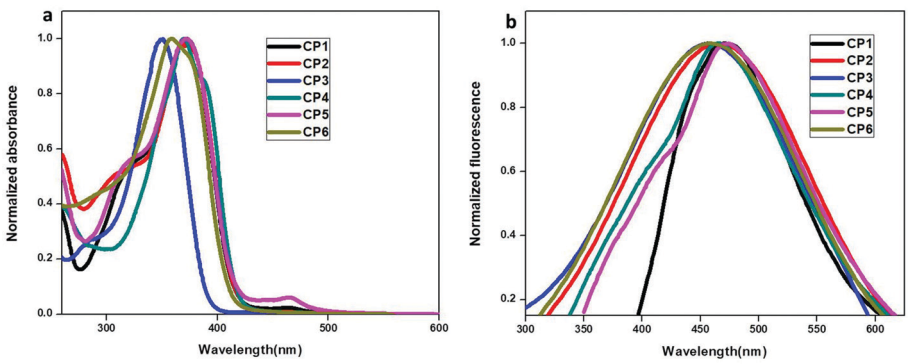

Fig. 1 Normalized absorbance and emission spectra of **CP1–CP6** in DMSO.

 This journal is © The Royal Society of Chemistry and the Centre National de la Recherche Scientifique 2021

Published on 15 March 2021. Downloaded by University of New Mexico on 5/16/2021 5:31:46 PM.

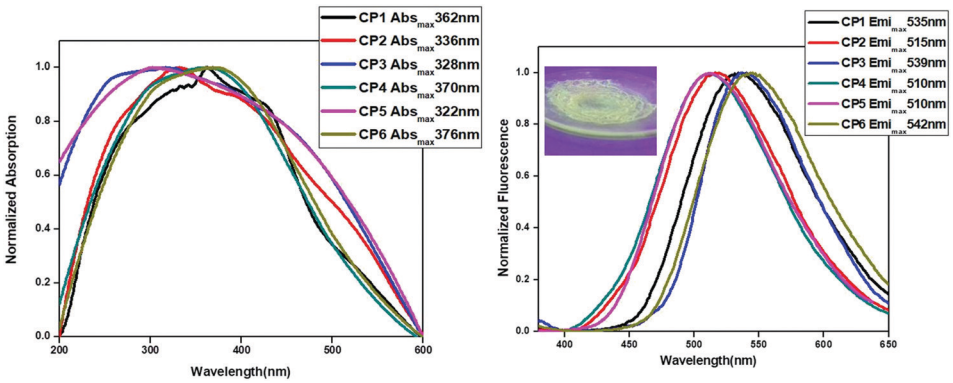

Fig. 2 Solid-state absorption and fluorescence of the compounds **CP1–CP6**; Insets: The fluorescence emissions of the solid for **CP1** under excitation at 362 nm.

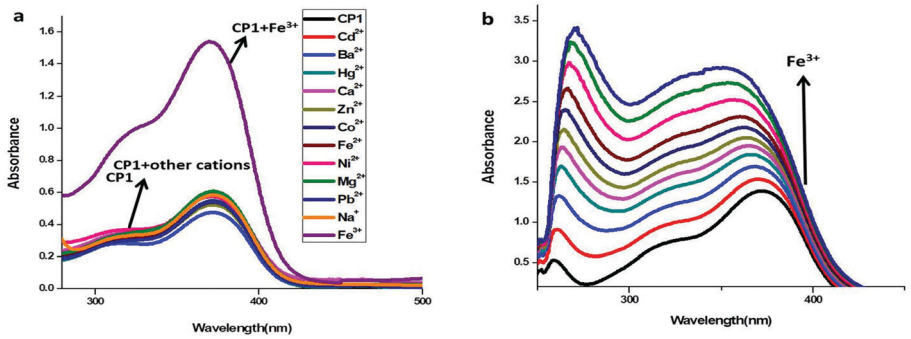

Fig. 3 (a) UV-Vis spectra of **CP1** in the presence of 2 equiv. of various cations. (b) Changes in UV spectra of **CP1** (1×10^{-4} M) as a function of Fe^{3+} (1×10^{-5} M) concentration.

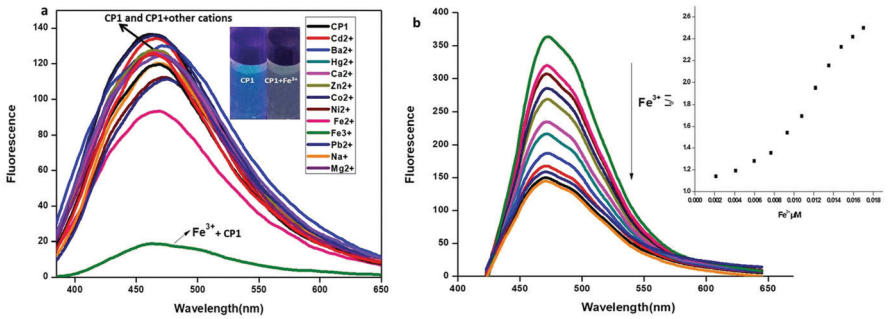

Fig. 4 (a) Emission spectra of **CP1** in the presence of 2 equiv. of various cations. (b) Changes in fluorescence spectra of **CP1** as a function of Fe^{3+} concentration; Inset: Stern–Volmer emission profile with the addition of Fe^{3+} to determine the limit of detection (LOD); [**CP1**] = 1×10^{-4} M, [Fe^{3+}] = 1×10^{-5} M.

The ESP (electrostatic potential) map of both the structures has been drawn to determine the nucleophilic and electrophilic behavior of the molecule. The region red in Fig. 6c is the electron-rich area, where the electrophilic attack occurs and the blue area indicates the electron-deficient region for the nucleophilic attack. The optimized structures and the ESP map of both the ligand and the complex are shown in Fig. 6. From Fig. 6, it is clear that the electronegative region is centered around the –CN nitrogen of the coumarin, nitrogen of the triazole, and oxygen of the carbonyl group connected to the pyrimidinone ring, and that constitutes the site for Fe^{3+} interaction.

The HOMO–LUMO energy gap calculations revealed that the maximum stability for the complex was obtained through the interaction of Fe^{3+} with the N of the CN group which is 3.2 eV, which is 1 eV less than that of the ligand **CP1** which is 4.2 eV. The energy gap obtained for the interaction of Fe^{3+} through the oxygen of the pyrimidinone is 6.68 eV, which is higher than that

Published on 15 March 2021. Downloaded by University of New Mexico on 5/16/2021 5:31:46 PM.

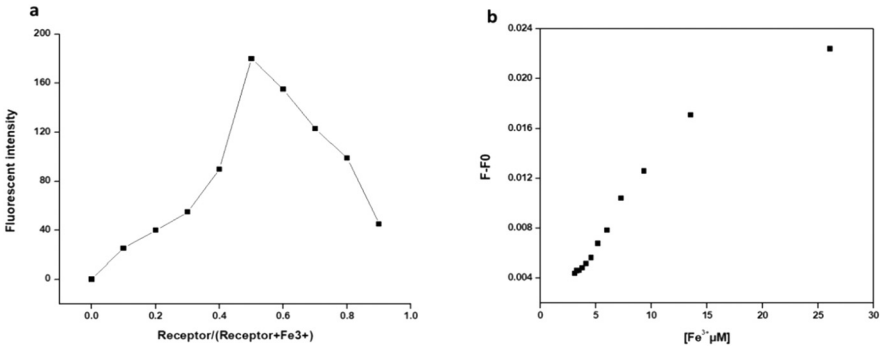

Fig. 5 (a) Job's plot for receptor Fe^{3+}, (b) Bensei–Hildebrand plot of the sensor **CP1** in the response of Fe^{3+}.

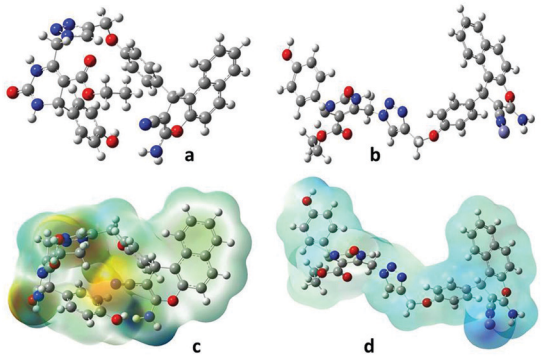

Fig. 6 (a and b): Optimized structures of ligand **CP1** and complex respectively; (c and d) ESP map of ligand and complex respectively.

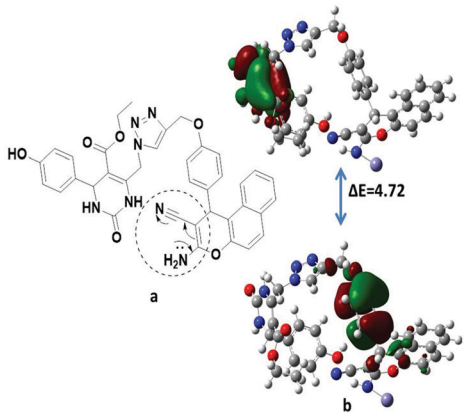

Fig. 7 (a) Resonance stabilization of the lone pair of electrons on the $-NH_2$ group with the ring. (b) Frontier molecular orbital and energy gap (ΔE) of **CP1** with Fe^{3+}, if the interaction of **CP1** is through NH_2 group.

of the parent ligand and the complex becomes unstable.[32] We didn't get any stable structures through the interaction of Fe^{3+} with the nitrogen of the triazole ring due to the absence of the lone pair of electrons on the nitrogen atoms for the interaction with Fe^{3+}, since it is preoccupied for conjugation in the triazole ring to make it aromatic. These observations were further validated by natural bond orbital (NBO) analysis[33–35] in which the lone pair of electrons on the nitrogen atom is found to be more spatially distributed than oxygen and also the energy of the former is higher than that of the latter. Similarly, the non-interaction of Fe^{3+} with amine group in the pyran was explained by theoretical studies as shown in Fig. 7. As shown in Fig. 7a, the lone pair of electrons in the $-NH_2$ group is in resonance stabilization with the –CN group. Hence, this lone pair is also not available for interaction with Fe^{3+}. The confirmation of this hypothesis was obtained from the calculation of the HOMO–LUMO energy gap of such an imaginary CP–Fe complex (Fig. 7b) proposed through the interaction of Fe with NH_2. The binding energy of this complex is obtained as 4.72 eV, which is higher than that of the ligand **CP1**. Hence the formation of such complex is not possible and the interaction of Fe^{3+} is only through the –CN group.

Before the attachment of the metal atom, the HOMO is primarily concentrated over the coumarin unit including cyano and amino groups, and the LUMO is spread over pyrimidinone and triazole rings. The interaction of the Fe^{3+} with **CP1** changes the electronic distribution in the complex as the HOMO spreads over the whole coumarin part excluding amino and cyano groups, whereas LUMO spreads over the iron atom, as shown in Fig. 8. The complexation of the ligand **CP1** with Fe^{3+} inhibits the ICT resulting in the quenching of the fluorescence. This makes **CP1** an efficient turnoff fluorescence sensor for the detection of Fe^{3+}. These computational explanations were also experimentally validated from the Fourier transform infrared (FT-IR) spectrum of **CP1** obtained in the presence and absence of Fe^{3+} (Fig. 9). From Fig. 9, it is clear that the CN band has a peak at 2227 cm^{-1} in **CP1** which is shifted to 2195 cm^{-1} due to its interaction with Fe^{3+} to form a stable complex.

In order to prove the selective nature of the probe in sensing Fe^{3+}, the fluorescence of the probe **CP1** in the presence of 0.5 equivalent of Fe^{3+} and an excess amount of (25 equivalents) other competing metal ions was observed (Fig. 10). As shown in Fig. 10, the tested metal ions show no interference for Fe^{3+}.

Demonstration of iron sensing for practical applications

Real sample experiments were carried out with distilled water and normal drinking water to check the practical applicability of the sensor **CP1** towards the fluorescence detection of Fe^{3+} ions. For this, we used a 1.0×10^{-4} M solution of **CP1** and a 1.0×10^{-5} M

 This journal is © The Royal Society of Chemistry and the Centre National de la Recherche Scientifique 2021

Published on 15 March 2021. Downloaded by University of New Mexico on 5/16/2021 5:31:46 PM.

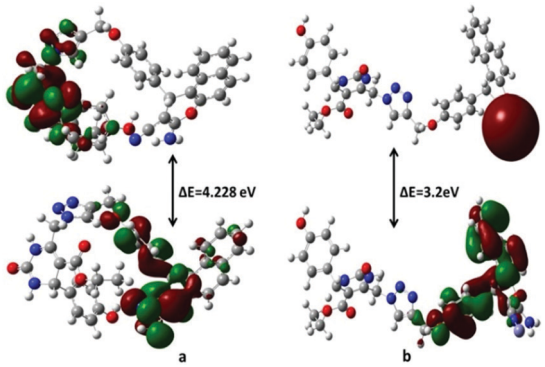

Fig. 8 Frontier molecular orbital and energy gap (ΔE) of (a) probe **CP1** and (b) **CP1** + Fe^{3+}.

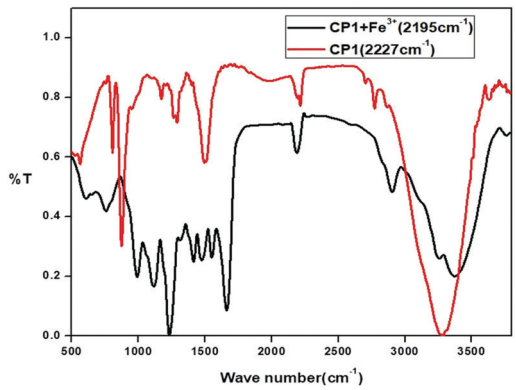

Fig. 9 FT-IR spectrum of **CP1** before and after the addition of Fe^{3+} ion.

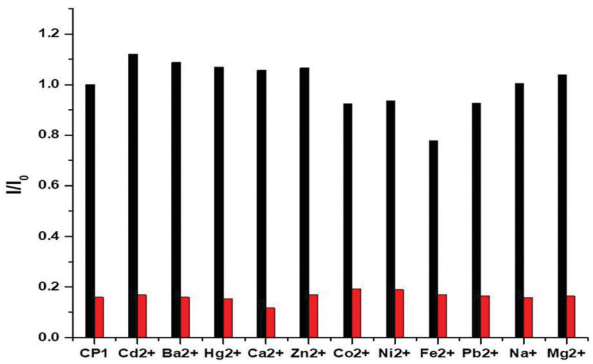

Fig. 10 Metal ion selectivity profiles of **CP1** (10^{-4} M): black bars, fluorescence of **CP1** in the absence and the presence of 25 equivalent Cd^{2+}, Ba^{2+}, Hg^{2+}, Ca^{2+}, Zn^{2+}, Co^{2+}, Ni^{2+}, Fe^{2+}, Pb^{2+}, Na^{+} and Mg^{2+} ions (10^{-5} M); red bars, fluorescence of **CP1** in the presence of various metal ions, followed by 0.5 equivalents of Fe^{3+} (10^{-5} M).

solution of Fe^{3+} in normal drinking water as well as in distilled water, and the results are shown in Fig. 11. From Fig. 11, it is clear that the sensing ability of **CP1** towards Fe^{3+} ions in distilled water shows good agreement with the same property obtained from normal drinking water. These experiments were repeated multiple

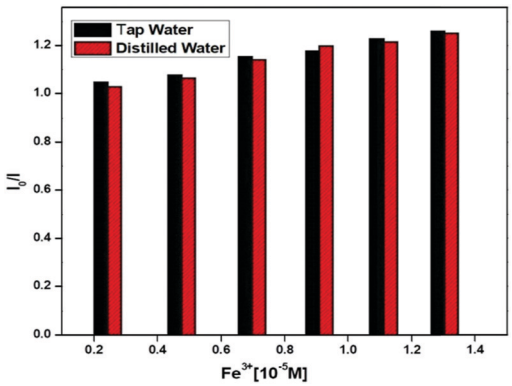

Fig. 11 Fluorescence signaling of Fe^{3+} ions by **CP1** in distilled water and normal drinking water.

times and the error obtained was within the acceptable limit (1–8%). The results indicate that our sensor molecule can be used for selective fluorescence detection (sensing) of Fe^{3+} ions in practical and industrial applications.

Binding modes of CP1–CP6 with biological protein CDK2

The drug property descriptors (molecular weight (M_W), log P, topological surface area, and the number of H bond donor and acceptor sites) of **CP1–CP6** were calculated using an online service, www.molinspiration.com.[36] The M_W of these molecules are in between 688.14 and 718.17, log P is in the range 4.5–6.02, and the topological surface area is between 166.43 and 212.25(for descriptor data: see ESI,† Table S1). According to Kihlberg's classification,[37,38] these molecules are in the extended rule of 5 (eRo5) class with the ability to bind with challenging or difficult to druggable biological targets. In the present study, cyclin-dependent kinase 2 (CDK2) was selected for studying the binding modes of **CP1–CP6** using AutoDockVina 1.1.2. The overexpression of CDK2 is one of the causes for different types of cancers such as cervical, colon, breast, ovarian, *etc.*[39,40] **CP1–CP6** showed strong hydrophobic interaction with CDK2 by embedding on its active sites through hydrogen bonding, van der Waals, and pi–cation interactions. The compound **CP1** showed one hydrogen bonding interaction between ASN132 and oxygen of the hydroxyl group in the benzene ring near the pyrimidine ring with a docking score of −9.8 kcal mol^{-1}. **CP2** fit in the active site of CDK2 (no H bonding) with a docking score of −9.6 kcal mol^{-1} whereas **CP3** interacts with CDK2 by pi–cation interaction between LYS89 and naphthalene ring with a docking score of −9.4 kcal mol^{-1}. **CP4** does not form any hydrogen bonds with CDK2 but is also well fitted in its active site with a binding score of −9.6 kcal mol^{-1}. **CP5** and **CP6** are also showed binding interactions with the protein by one hydrogen bonding in addition to the hydrophobic interaction. The hydrogen bonding interaction in **CP5** is between ASP145 and oxygen of the NO_2 on the pyrimidinone part with a high binding energy of −9.6 kcal mol^{-1} whereas in **CP6** the bonding is between THR14 and oxygen of the carbonyl group in the pyrimidinone ring with a binding score of −9.5 kcal mol^{-1}. The docking scores are listed in Table S2 (see ESI†) and the binding modes are presented in Fig. S1(see ESI†).

Published on 15 March 2021. Downloaded by University of New Mexico on 5/16/2021 5:31:46 PM.

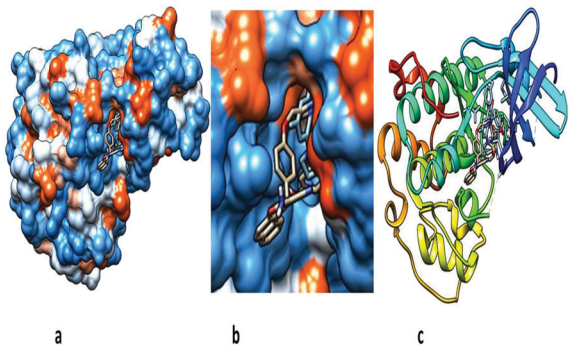

Fig. 12 (a) Hydrophobic interaction of **CP1** with CDK2 protein, b; its enlarged portion, c; its cocrystal structure. (b) Changes in UV spectra of **CP1** (1×10^{-4} M) as a function of Fe^{3+} (1×10^{-5} M) concentration.

The hydrophobic interaction of **CP1** (having the highest docking score) with CDK2 and its cocrystal structures are presented in Fig. 12. From this discussion, it is clear that after the docking of the probe molecules on the active sites of CDK2 through hydrophobic interactions, their hydrophilic binding sites are intact and are available for complexation with endogenous Fe^{3+}. This shows the potential of the new probe molecules as efficient Fe sensors and therapeutic agents for addressing cancers or other diseases caused by iron overloading (iron-loading anemia).

Cytotoxicity of CP1 against the human cervical cancer cell line (HeLa)

As a proof of concept, the molecule **CP1** with the highest docking score has been selected for evaluating its cytotoxicity against the human cervical cancer cell line (HeLa) to show the potential of this sensor as an efficient therapeutic too. The cytotoxic evaluation has been carried out by MTT assay. Fig. S2a (ESI†) shows the *in vitro* cytotoxic activity of the compound **CP1** (1.5, 3, 6, 9, 12, 15, 18, 21, 27, 30 μg mL^{-1} concentrations, in PBS, pH 7.4), against the HeLa cells. The IC50 values of **CP1** against HeLa cells were calculated as 15 μg mL^{-1} (in 48 h). The morphology of the HeLa cells in the presence and absence of the **CP1** was also studied by using inverted phase-contrast microscopy as shown in Fig. S2b (ESI†). The cells treated with **CP1** were different from the control. In control, the cells were closely packed whereas irregular cell membranes were observed when HeLa cells were treated with **CP1** at IC25 and IC50, and the observation serves as apparent evidence for apoptotic activation.

Conclusion

In summary, an array of chromene–pyrimidine triad based efficient chemosensor therapeutics have been developed for a broad spectrum of applications such as detection of Fe^{3+} present in biological environments, targeting and annihilation of iron loaded anemia, and water purification. The therapeutic sensors were designed and synthesized through the sequential use of green synthetic methodologies marking its ease and cost effectiveness. Structural components of the chemosensors are based on naturally occurring/biological molecules such as chromene and pyrimidine, which also illustrate their bio- and environmental compatibility. The sensor molecules showed selective and sensitive turn-off fluorescence with Fe^{3+} by forming a stable complex with the chemosensor with an extremely low limit of detection. The docking studies with biological protein CDK2 showed the potential of these new molecules as therapeutic sensors. This was further illustrated with the cytotoxicity studies against the human cervical cancer cell line HeLa which showed a very low IC50 value of 15 μg mL^{-1}. These promising results can be further explored for the development of efficient chemosensor therapeutics for a broad spectrum of applications.

Author contributions

All authors conceived and planned the experiments. A. S. performed the experiments, contributed to the analysis, and drafted the manuscript. D. B. contributed to the analysis and edited the manuscript. All authors read and approved the final manuscript.

Conflicts of interest

The authors declare no conflict of interest.

Acknowledgements

A. S. thanks the University Grants Commission (UGC), New Delhi, for the research fellowship. The authors wish to thank the Central Instrumentation Facility (CIF), University of Calicut, Kerala, India for providing the computational facilities.

Notes and references

1 B. J. Crielaard, T. Lammers and S. Rivella, *Nat. Rev. Drug Discovery*, 2017, **16**, 400–423.
2 T. U. Kumar, S. Pawar, A. Nag and A. Bhattacharya, *J. Fluoresc.*, 2019, **29**, 271–277.
3 K. Jomova and M. Valko, *Curr. Pharm. Des.*, 2011, **17**, 3460–3473.
4 D. Coghill, T. Banaschewski, A. Zuddas, A. Pelaz, A. Gagliano and M. Doepfner, *BMC Psychiatry*, 2013, **13**, 237.
5 R. R. Crichton, D. T. Dexter and R. J. Ward, *Coord. Chem. Rev.*, 2008, **252**, 1189–1199.
6 M. Gu, A. D. Owen, S. E. K. Toffa, J. M. Cooper, D. T. Dexter, P. Jenner, C. D. Marsden and A. H. V. Schapira, *J. Neurol. Sci.*, 1998, **158**, 24–29.
7 A. S. Dornelles, V. A. Garcia, M. N. M. de Lima, G. Vedana, L. A. Alcalde, M. R. Bogo and N. Schröder, *Neurochem. Res.*, 2010, **35**, 564–571.
8 S. Devaraj, Y. Tsui, C.-Y. Chiang and Y.-P. Yen, *Spectrochim. Acta, Part A*, 2012, **96**, 594–599.
9 E. C. Theil and D. J. Goss, *Chem. Rev.*, 2009, **109**, 4568–4579.
10 S. K. Sahoo, D. Sharma, R. K. Bera, G. Crisponi and J. F. Callan, *Chem. Soc. Rev.*, 2012, **41**, 7195–7227.
11 T. Puthiyedath and D. Bahulayan, *Sens. Actuators, B*, 2018, **272**, 110–117.

 This journal is © The Royal Society of Chemistry and the Centre National de la Recherche Scientifique 2021

Published on 15 March 2021. Downloaded by University of New Mexico on 5/16/2021 5:31:46 PM.

12 T. Puthiyedath and D. Bahulayan, *Sens. Actuators, B*, 2017, **239**, 1076–1086.
13 A. C. Boukis, K. Reiter, M. Frölich, D. Hofheinz and M. A. R. Meier, *Nat. Commun.*, 2018, **9**, 1439.
14 A. Dömling, W. Wang and K. Wang, *Chem. Rev.*, 2012, **112**, 3083–3135.
15 F. Y. Thanzeel, K. Balaraman and C. Wolf, *Nat. Commun.*, 2018, **9**, 5323.
16 Y. H. Lau, P. J. Rutledge, M. Watkinson and M. H. Todd, *Chem. Soc. Rev.*, 2011, **40**, 2848–2866.
17 B.-R. Gao, H.-Y. Wang, Y.-W. Hao, L.-M. Fu, H.-H. Fang, Y. Jiang, L. Wang, Q.-D. Chen, H. Xia and L.-Y. Pan, *et al.*, *J. Phys. Chem. B*, 2010, **114**, 128–134.
18 Y. Dong, Z. Yang, Z. Ren and S. Yan, *Polym. Chem.*, 2015, **6**, 7827–7832.
19 L. Wang, D. Wang, H. Lu, H. Wang, L. Xue and S. Feng, *Appl. Organomet. Chem.*, 2013, **27**, 529–536.
20 Q. Zhao, S. Zhang, Y. Liu, J. Mei, S. Chen, P. Lu, A. Qin, Y. Ma, J. Z. Sun and B. Z. Tang, *J. Mater. Chem.*, 2012, **22**, 7387–7394.
21 S. Kaur, M. Kumar and V. Bhalla, *Chem. Commun.*, 2015, **51**, 4085–4088.
22 B.-K. An, D.-S. Lee, J.-S. Lee, Y.-S. Park, H.-S. Song and S. Y. Park, *J. Am. Chem. Soc.*, 2004, **126**, 10232–10233.
23 D. Oelkrug, A. Tompert, J. Gierschner, H.-J. Egelhaaf, M. Hanack, M. Hohloch and E. Steinhuber, *J. Phys. Chem. B*, 1998, **102**, 1902–1907.
24 B.-K. An, S.-K. Kwon, S.-D. Jung and S. Y. Park, *J. Am. Chem. Soc.*, 2002, **124**, 14410–14415.
25 H. Wang, E. Zhao, J. W. Y. Lam and B. Z. Tang, *Mater. Today*, 2015, **18**, 365–377.
26 F. Würthner, T. E. Kaiser and C. R. Saha-Möller, *Angew. Chem., Int. Ed.*, 2011, **50**, 3376–3410.
27 Z. He, C. Ke and B. Z. Tang, *ACS Omega*, 2018, **3**, 3267–3277.
28 Y. Hong, J. W. Y. Lam and B. Z. Tang, *Chem. Soc. Rev.*, 2011, **40**, 5361–5388.
29 M. Kádár, A. Biró, K. Tóth, B. Vermes and P. Huszthy, *Spectrochim. Acta, Part A*, 2005, **62**, 1032–1038.
30 R. Wang and Z. Yu, *Acta Phys.-Chim. Sin.*, 2007, **23**, 1353–1359.
31 M. J. Frisch, *et al.*, *Gaussian 09, Revision A.01*, Gaussian, Inc., Wallingford CT, 2009.
32 A. Shylaja, S. S. Roja, R. V. Priya and R. R. Kumar, *J. Org. Chem.*, 2018, **83**, 14084–14090.
33 S. Joshi, S. Kumari, R. Bhattacharjee, A. Sarmah, R. Sakhuja and D. D. Pant, *Sens. Actuators, B*, 2015, **220**, 1266–1278.
34 A. E. Reed, L. A. Curtiss and F. Weinhold, *Chem. Rev.*, 1988, **88**, 899–926.
35 A. E. Reed, R. B. Weinstock and F. Weinhold, *J. Chem. Phys.*, 1985, **83**, 735–746.
36 C. J. Gerry and S. L. Schreiber, *Nat. Rev. Drug Discovery*, 2018, **17**, 333.
37 S. Hsiung, M. Adlersberg, V. Arango, J. J. Mann, H. Tamir and K. Liu, *J. Neurochem.*, 2003, **87**, 182–194.
38 B. C. Doak, J. Zheng, D. Dobritzsch and J. Kihlberg, *J. Med. Chem.*, 2016, **59**, 2312–2327.
39 M. Mihara, S. Shintani, Y. Nakahara, A. Kiyota, Y. Ueyama, T. Matsumura and D. T. W. Wong, *Jpn. J. Cancer Res.*, 2001, **92**, 352–360.
40 M. Marone, G. Scambia, C. Giannitelli, G. Ferrandina, V. Masciullo, A. Bellacosa, P. Benedetti-Panici and S. Mancuso, *Int. J. Cancer*, 1998, **75**, 34–39.